

Finite difference synthesis of infrasound propagation through a windy, viscous atmosphere: Application to a bolide explosion detected by seismic networks

Catherine de Groot-Hedlin, Michael A.H. Hedlin, and Kris Walker

Laboratory for Atmospheric Acoustics, Institute of Geophysics and Planetary Physics,
Scripps Institution of Oceanography, University of California, San Diego, La Jolla, CA

Original form: June 26, 2010

Revised: December 14, 2010

In press: Geophysical Journal International

Abstract:

A finite-difference time-domain (FDTD) algorithm has been developed to model linear infrasound propagation through a windy, viscous medium. The algorithm has been used to model signals from a large bolide that burst above a dense seismic network in the US Pacific Northwest on 19 February, 2008. We compare synthetics that have been computed using a G2S-ECMWF atmospheric model to signals recorded at the seismic networks located along an azimuth of 210° from the source; the results show that the timing and the range extent of the direct, stratospherically ducted and thermospherically ducted acoustic branches are accurately predicted. However, estimates of absorption obtained from standard attenuation models (Sutherland-Bass) predict much greater absorption for thermospheric returns at frequencies greater than 0.1 Hz than is observed. We conclude that either the standard absorption model for the thermosphere is incorrect, or that thermospheric returns undergo non-linear propagation at very high altitude. In the former case, a better understanding of atmospheric absorption at high altitudes is required; in the latter, a fully nonlinear numerical method is needed to test our hypothesis that higher frequency arrivals from the thermosphere result from nonlinear propagation at thermospheric altitudes.

Keywords: Acoustic properties, Wave propagation, Numerical solutions, Numerical approximations and analysis, North America

I. INTRODUCTION

The study of infrasound – sub-audible acoustic energy - has undergone enormous advances since the first reports of barometric fluctuations observed worldwide after the eruption of Krakatoa (see Evers & Haak, 2010 for a review). Early advances in infrasound studies were motivated by the utility of low frequency sounds for estimating gradients in wind and temperatures to high altitudes (eg. Gutenberg 1939). After World War II, progress in infrasound was driven by the need to monitor the Earth and atmosphere for clandestine nuclear tests. Ultimately, this led to the construction of a global network of infrasound stations (Christie and Campus, 2010), which is being deployed as one component of the International Monitoring System (IMS) and is designed to monitor nuclear explosions. Many natural sources are also detected at this network so that its development has rekindled interest in the use of infrasound to examine a wide variety of atmospheric and geophysical phenomena, including ocean swell (Garces *et al* 2003; Hetzer *et al* 2010), ocean surf (Arrowsmith & Hedlin, 2005), tsunamis (Le Pichon *et al* 2005a), earthquakes (Le Pichon *et al* 2006; Mutschlechner & Whitaker 2010), volcanoes (Matoza *et al* 2006; Fee & Garces 2007; Matoza *et al* 2009), and meteors (Revelle *et al* 2004; Edwards 2010).

Although the global IMS stations are augmented by several dozens of regional arrays worldwide, the infrasound network remains sparse compared to typical seismic networks. To compensate for gaps in spatial coverage, a number of infrasound studies have used presumed air-to-ground coupled arrivals recorded on seismometers to examine the infrasound wavefield in detail. Acoustic arrivals from the explosion of the December 2005 Buncefield oil depot, in the UK, were recorded at infrasound arrays and seismometers across central Europe. Atmospheric ray-tracing confirmed that arrivals were associated with ducting through the troposphere, stratosphere, and the thermosphere (Ottemöller & Evers 2008; Ceranna *et al* 2009). Tropospheric and stratospheric arrivals generated by the descent of the shuttle Atlantis over southern California in June of 2007 were detected at over 100 seismometers associated with the transportable USArray network and other regional networks (de Groot-Hedlin *et al* 2008). More recently, a bolide explosion in northeastern Oregon in February of 2008 generated tropospheric, stratospheric, and thermospheric arrivals that were detected at 4 infrasound arrays in Canada and the US and by 500 seismic stations in the US Pacific Northwest (Hedlin *et al* 2010).

The efficacy of infrasound for remotely sensing natural and anthropogenic hazards stems from the excellent transmission characteristics of low frequency acoustic signals through the atmosphere. Both tropospheric and stratospherically ducted infrasound undergo minimal absorption within the atmosphere; the former depend mainly on diurnal sound and wind speed variations, while the latter depend on seasonally-varying stratospheric winds. As a result, detection rates of stratospherically ducted infrasound varies seasonally, which has implications for the detection thresholds of the IMS infrasound network (Le Pichon *et al* 2009).

Thermospheric signals, which propagate between the ground and lower thermosphere, may be the only infrasound arrivals. They are predicted in every direction, for all seasons, due to the steep sound speed gradients at altitudes over 90 km. However, infrasound signals along this path are thought to be highly attenuated due to enhanced absorption within the thin air of the upper atmosphere so that only very large infrasound sources generate detectable thermosphericly refracted arrivals. Thermospheric signals generated by large volcanic eruptions (Evers and Haak 2005; Le Pichon *et al* 2005b; Le Pichon *et al* 2005c) and the Buncefield vapor cloud explosion (Ceranna *et al* 2009) have been detected at infrasound arrays.

The Buncefield explosion (Ottemöller & Evers 2008; Ceranna *et al* 2009) and a bolide terminal burst (Hedlin *et al* 2010) generated thermospheric signals that were detected as air-to-ground coupled arrivals at seismic stations.

A combined analysis of stratospheric and thermospheric arrivals generated by a single large source may provide tighter constraints on source characteristics of very large explosions (Whitaker & Mutschlecner 2008). However, a problem with relying on detections of thermospheric arrivals is that wind and sound speeds above about 50 km are poorly constrained. The current standard in atmospheric specifications is to fuse operational weather analysis - which is updated several times daily - within the troposphere and stratosphere, with empirical climatologies above (Drob *et al* 2003; Picone *et al* 2002). A further difficulty is that acoustic absorption is also poorly constrained at high altitudes. Attenuation values have been predicted for altitudes up to 160 km, but estimates above 90 km are imprecise due to uncertainties about atmospheric composition (Sutherland & Bass 2004).

The development of more precise estimates of thermospheric attenuation have been hampered both by the low density of infrasound stations, and the lack of waveform synthesis methods that handle infrasound attenuation. The utility of USArray seismic stations for recording infrasound signals has lessened the first problem. However, numerical methods that include the effects of both wind and attenuation are needed in modeling infrasound propagation at altitudes over 50 km. In previous efforts, the effect of wind has been introduced into a parabolic equation modeling algorithm (Lingevitch *et al* 2002) and finite difference time domain (FDTD) methods (Ostashev *et al* 2005; Van Renterghem and D. Botteldoren 2003). In frequency-domain modeling methods, like parabolic equation (PE) or fast field program (FFP) methods (e.g. Jensen *et al* 1994), attenuation is introduced by adding a small, non-physical, imaginary term to the acoustic velocity. An acoustic viscosity term was introduced directly into the governing equations of an FDTD algorithm (de Groot-Hedlin 2008). This method yields attenuation values that increase with the square of the frequency, in agreement with theory (Sutherland & Bass, 2004).

In this paper, we introduce an FDTD algorithm that includes both wind and attenuation and apply it to explain infrasound arrivals, including thermospheric arrivals, generated by a terminal bolide explosion that occurred over northeastern Oregon on February 2008 (Hedlin *et al* 2010; Walker *et al* 2010). Air-to-ground coupled arrivals were recorded at five hundred broadband seismic stations of the USArray and regional networks including the Wallowa Flexible Array network and the High Lava Plains Seismic Experiment, which were deployed to investigate crustal and upper mantle structure of the region. In Hedlin *et al* (2010), 3-D atmospheric ray-tracing was used to identify arrivals as tropospherically, stratospherically, or thermospherically ducted; the results confirmed that late arrivals to the southwest of the bolide explosion were associated with thermospheric returns. The source time and location of the terminal burst were determined by a combination of video observations, infrasound arrays, back projecting USArray seismic waveform envelopes, and modeling the timing of direct arrivals at 13 seismic stations located within a 87 km radius of the burst (Walker *et al* 2010). The high signal-to-noise ratios of the thermospheric arrival at many receivers, together with accurate source parameter estimates, allow us to test our newly developed FDTD infrasound propagation algorithm on real data. We show that our synthetic modeling results - based on current knowledge of atmospheric sound speeds, wind speeds, and attenuation - agree with observed infrasound signals to first order.

This paper is structured as follows. The linearized equations governing acoustic wave propagation in a windy, absorptive medium are derived in the next section. A finite difference time domain (FDTD) approach to solving these equations in a stratified, range independent medium is presented in the Section III. Section IV shows the application of the method to data from the bolide. In Section V we discuss differences between the observed data and synthesized results, with implications for acoustic propagation and absorption in the thermosphere. Section VI gives concluding remarks.

II. Linear Infrasound Propagation in a Windy, Absorptive Medium

The energy dissipation that occurs during any fluid motion, including fluctuations associated with acoustic propagation, affects that motion. At infrasonic frequencies and altitudes over 60 km, internal friction (viscosity) is the dominant absorption mechanism; at lower altitudes, infrasound absorption is dominated by molecular vibration losses, which involves the excitation of gas molecules comprising the atmosphere (Sutherland & Bass 2004). However, the latter absorption mechanism leads to losses of less than about 10^{-5} dB/km at infrasonic frequencies and thus is neglected here. Therefore, in this paper we consider only absorption losses caused by atmospheric viscosity. Although the energy dissipation is irreversible, we also apply the standard assumption of isentropy, that is, that entropy of the wave motion remains unchanged. More precisely, some dissipation of energy occurs in the presence of viscosity, but it can be shown that this is only a second order effect, and may therefore be neglected for linear propagation modeling.

In this section, we derive coupled equations for infrasound propagation through a windy, viscous atmosphere. The equation for the acoustic pressure fluctuations p

$$\frac{Dp}{Dt} = -\rho c^2 \nabla \cdot \bar{V}, \quad (1)$$

derived by combining the equations of state and conservation of mass, relates the total particle velocity, \bar{V} , density, ρ , and sound speed c to the advective derivative of the pressure, where the advective derivative is given by $D/Dt = \partial/\partial t + \bar{V} \cdot \nabla$. The Navier-Stokes equation for a compressible viscous fluid gives the acoustic particle velocity

$$\rho \frac{D\bar{V}}{Dt} = -\nabla p + \eta \nabla^2 \bar{V} + \left(\zeta + \frac{\eta}{3}\right) \nabla(\nabla \cdot \bar{V}) + \bar{f}, \quad (2)$$

(Eq. 15.6 of Landau & Lifshitz 1959) where \bar{f} is an external source acting upon the medium, η is called the viscosity coefficient and ζ is variously called the second, volume, or bulk viscosity. The term $\nabla^2 \bar{V}$ denotes the vector $[\nabla^2 V_x, \nabla^2 V_y, \nabla^2 V_z]$. Both viscosity coefficients vary only slightly in the atmosphere; in fact, this was assumed in the derivation of Eq. 2 (Landau & Lifshitz 1959). The value of η for air is approximately 1.8×10^{-5} kg m⁻¹s⁻¹ and the bulk viscosity ζ is usually of the same order of magnitude (Landau & Lifshitz 1959); Pierce (1981) gives $\zeta = 0.6\eta$. However, the bulk viscosity is often omitted (e.g. de Groot-Hedlin 2008; Gill 1982).

The pressure, density, and velocity fields fluctuate due to the propagation of a sound wave within a medium. The pressure, density and velocity fields are expressed as the sums of their ambient values and perturbations caused by the passage of a sound wave:

$$p = p_o + p_s; \quad \rho = \rho_o + \rho_s; \quad \vec{V} = \vec{w} + \vec{v} \quad (3)$$

where the ambient pressure and density values are denoted by the o subscript, and s denotes perturbations caused by passage of a sound wave. Here \vec{w} denotes the wind speed and \vec{v} is the acoustic particle velocity. Waveforms are derived by computing the pressure fluctuations as a function of time.

Equations 3 are inserted into Eqs. 1 and 2 in order to derive a set of linear partial differential equations for the pressure and particle velocities. It is assumed that the background field is in stable equilibrium, *i.e.* that Eqs. 1 and 2 are satisfied in the absence of a sound wave, so that zeroth order terms cancel. Only linear terms in the pressure, density and particle velocities are retained, under the assumption that pressure and density fluctuations due to the passage of a sound wave are only a small fraction of the ambient values, and that the particle velocities are small compared to the sound speed. We also assume that $\nabla \rho_o = \nabla p_o = 0$ which is valid at typical infrasound frequencies where buoyancy waves are insignificant, *i.e.* we consider only frequencies greater than 3 mHz (Lingevitch *et al* 1999). If it is assumed that the divergence in the wind speed is negligible (*i.e.* $\nabla \cdot \vec{w} = 0$), as in Ostashev *et al* (2005), Eq. 1 becomes

$$\frac{\partial p_s}{\partial t} = -\vec{w} \cdot \nabla p_s - \rho_o c^2 \nabla \cdot \vec{v}. \quad (4)$$

Over large scales, it is assumed that vertical component of wind is negligible compared to the horizontal components and so is set to zero in the G2S models often used for computation of infrasound propagation (Drob *et al* 2003). Therefore in the following, we assume that winds are horizontal and that wind gradients are only vertical. Then Eq. 2 yields

$$\frac{\partial \vec{v}}{\partial t} = -(\vec{v} \cdot \nabla) \vec{w} - (\vec{w} \cdot \nabla) \vec{v} + \frac{1}{\rho_o} \left(-\nabla p_s + \eta \nabla^2 (\vec{v} + \vec{w}) + \left(\zeta + \frac{\eta}{3} \right) \nabla (\nabla \cdot \vec{v}) \right) + \vec{f}. \quad (5)$$

For horizontal winds that vary with altitude, $\nabla^2 \vec{w} = \left[\frac{\partial^2 w_x}{\partial z^2}, \frac{\partial^2 w_y}{\partial z^2}, 0 \right]$. Note that terms involving fluctuations in the atmospheric density ρ_s drop out of the equations when gravity is neglected. Equations 4 and 5 are the governing equations for infrasound propagation in a viscous, windy atmosphere; a numerical method of infrasound waveform synthesis for a general model with varying densities, and sound and wind speeds is described in the next section.

In the remainder of this section, we derive an analytic expression for the pressure wavefield for a highly simplified model in which the density and sound speed are uniform, and there is no wind. In this way, we demonstrate that the inclusion of the viscosity terms into the propagation equations leads to the attenuation and dispersion of the computed acoustic arrivals. In this case Eqs. 4 and 5 may be combined to yield a single analytic expression:

$$\frac{\partial^2 p_s}{\partial t^2} = c^2 \left(1 + q \frac{\partial}{\partial t} \right) \nabla^2 p_s, \quad (6)$$

where

$$q = \left[\frac{4\eta}{3} + \zeta \right] / \rho_o c^2 \quad (7)$$

Equation (6) describes a medium in which internal viscosity is the dominant absorption mechanism (Lighthill 1978).

We insert a trial plane wave solution of the form

$$p_s(\vec{r}, t) \propto e^{i(\vec{k} \cdot \vec{r} - \omega t)} \quad (8)$$

into eq. (6) where ω is the circular frequency, \vec{r} is the vector distance, and t is the time, to solve for the wave number \vec{k} . We obtain the complex-valued, squared wavenumber

$$\vec{k}^2 = \frac{\omega^2}{c^2(1 - i\omega q)}. \quad (9)$$

The wavenumber is related to the frequency dependent wave speed c_p and attenuation α through $k(\omega) = \omega/c_p(\omega) + i\alpha(\omega)$. We write $k^2(\omega)$ in exponential notation as $k^2 = |k^2|e^{i\phi}$, where ϕ is the argument of k^2 to derive

$$\frac{\omega}{c_p} = \text{Re}(k) = \sqrt{|k^2|} \cos(\phi/2) \quad (10a)$$

and

$$\alpha = \text{Im}(k) = \sqrt{|k^2|} \sin(\phi/2). \quad (10b)$$

Applying trigonometric half-angle formulas, it can be shown after some algebraic manipulation that the expression for the frequency dependent sound speed is given by

$$c_p(\omega) = c \sqrt{\frac{2(1 + q^2\omega^2)}{1 + \sqrt{1 + q^2\omega^2}}}, \quad (11)$$

and the expression for atmospheric attenuation is given by

$$\alpha(\omega) = \frac{\omega}{\sqrt{2}c} \sqrt{\frac{\sqrt{1 + q^2\omega^2} - 1}{(1 + q^2\omega^2)}}. \quad (12)$$

Equations 11, 12, and 7 imply that phase velocities and attenuation are dependent on the coefficients of attenuation, static sound speeds, and atmospheric density. Throughout the infrasound range, *i.e.* up to frequencies of 20 Hz, and at altitudes below 100 km, $q\omega \ll 1$, so the dispersion relation and attenuation may be approximated as

$$c_p(\omega) \approx c \left(1 + \frac{3}{8}q^2\omega^2\right) \quad (13)$$

and

$$\alpha(\omega) \approx \frac{q\omega^2}{2c} (1 - q^2\omega^2/2). \quad (14)$$

Equations 13 and 14 indicate that both dispersion and attenuation are approximately proportional to the square of the frequency for $q\omega \ll 1$; Eq. 7 implies that both values increase with decreasing density. Since the atmospheric density decreases exponentially in the atmosphere, high frequencies are increasingly attenuated and dispersed in the Earth's upper

atmosphere. Consequently, sound waves refracted within the thermosphere should be dispersed and have less power at higher frequencies than those refracted at lower altitudes.

Atmospheric sound speeds and densities vary over scale lengths much longer than the infrasound wavelength, thus Eqs. 11 and 12 may be used to derive infrasound attenuation and phase speeds for a stratified atmosphere with slowly changing sound speed and density variations. Figure 1 shows the attenuation and dispersion derived from Eqs. 11 and 12 for a sound speed profile in northeastern Oregon on the morning of 19 February 2008. This profile is relevant to a bolide explosion that will be examined in greater detail in Section IV. The atmospheric density profile, also shown in Figure 1, is derived using the hydrostatic equation for pressure gradients combined with the ideal gas law relating density and temperature to pressure, and $c^2 = kRT$, relating sound speed and temperature T ($k=1.4$ is the ratio of specific heats, and $R = 287.04 \text{ J kg}^{-1} \text{ K}^{-1}$ is the gas constant for dry air).

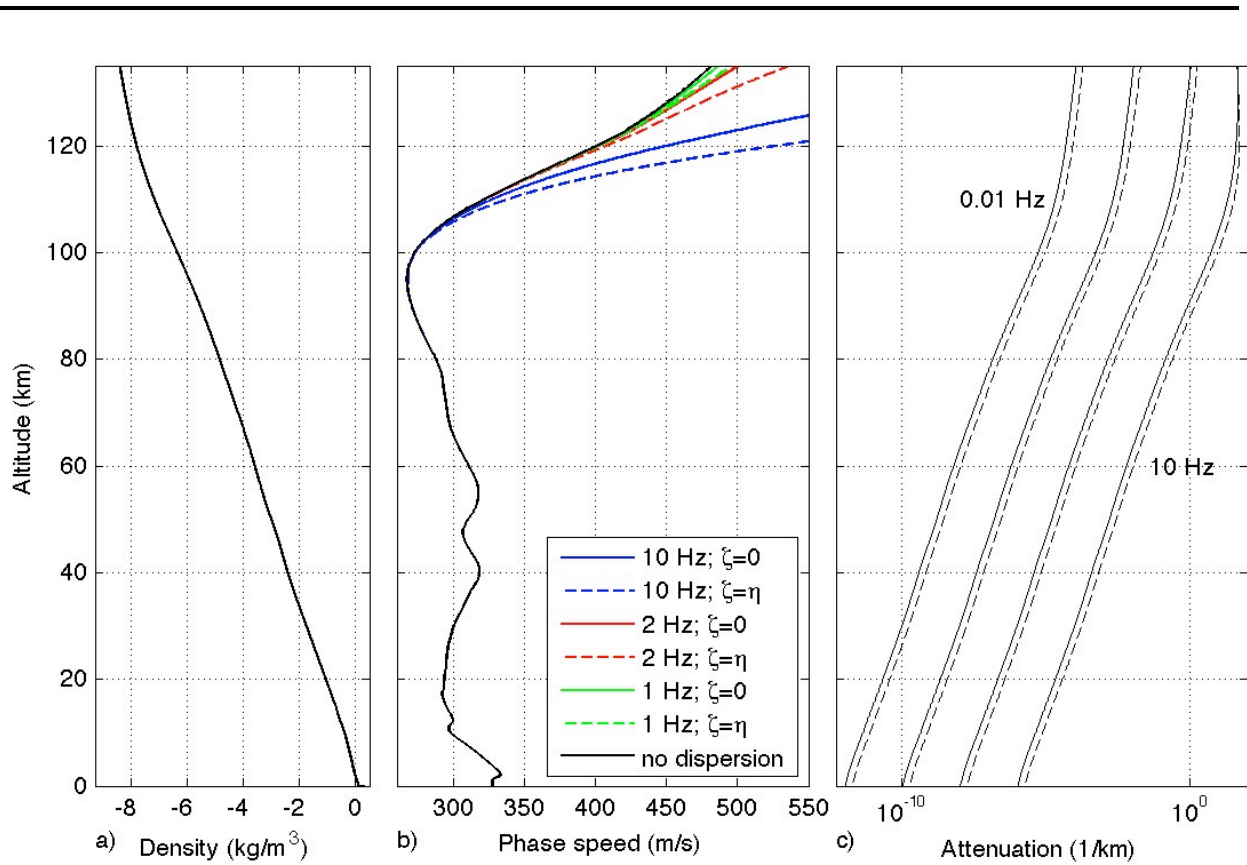


Figure 1. a) Atmospheric density profile corresponding to the static sound speed profile in b. b) Static sound speed profile (black) and phase speed profiles computed for several infrasound frequencies. Phase speeds have been computed for $\zeta = \eta = 1.8 \times 10^{-5} \text{ kg m}^{-1} \text{ s}^{-1}$, and for $\zeta = 0$. c) Attenuation coefficients $\alpha(\omega)$ computed at frequencies of 0.01, 0.1, 1, and 10 Hz, for $\zeta = \eta = 1.8 \times 10^{-5} \text{ kg m}^{-1} \text{ s}^{-1}$ (dashed lines), and for $\zeta = 0$ (solid lines).

Figure 1 shows that there is significant dispersion at the upper end of the infrasound frequency range. Phase speeds are significantly higher than the static sound speeds at an altitude of 120 km and a frequency of 10 Hz. As a result, acoustic energy at this frequency would be mostly refracted downward and little energy could penetrate to higher altitudes. At lower frequencies, infrasound energy can propagate to higher altitudes but undergoes significant absorption as shown in Fig 1c. Below 1 Hz, phase speeds are nearly identical to static sound speeds at altitudes below 125 km so that dispersion would be negligible. An alternative method of deriving the velocity dispersion (Bass *et al*, 2007) yields similar dispersion values up to 120 km at infrasound frequencies; at higher altitudes, their results suggest greater dispersion.

The attenuation values shown in Figure 1c are similar to those derived from the formulae in Sutherland & Bass (2004) at altitudes above 60 km, reflecting the fact that viscosity is the dominant loss mechanism at high altitudes. The attenuation values at lower altitudes are smaller, reflecting the fact that other loss mechanisms that dominate at lower altitude are neglected here. However, as previously stated these losses are negligible at infrasound frequencies.

III. NUMERICAL IMPLEMENTATION

A. The Finite Difference Time Domain (FDTD) approach

Equations 4 and 5 form a complete set of coupled equations for the pressure and acoustic particle velocity, given ambient values for the atmospheric sound speeds, wind velocities, and attenuation constants. These equations are amenable to solution by the FDTD approach, which is based on replacing the spatial and time derivatives in the governing equations by their difference approximations. The pressure and particle velocities may then be computed over a set of discrete nodes that comprise the spatial and temporal grids.

This method of solution is presented here for two-dimensional (2D) models, using a staggered spatial grid as shown in Figure 2. In 2D, the model is divided into a grid of cells of dimension Δx by Δz , each with a uniform density ρ_0 and static sound speed c . Pressure variables are sampled at the center of each cell and the particle velocity components are sampled at points along the cell boundaries. The primary advantage of using the spatially staggered grid is that it provides centered spatial differences for many of the derivatives in the FDTD implementation, which are accurate to second order, rather than forward or backward differences, which are accurate only to first order. Higher order spatial or temporal finite difference methods are available which would lead to equivalent accuracy with a coarser grid sampling than is used with the simple central difference operators applied here. However, the objective here is to demonstrate the applicability of the FDTD method for simulating infrasound propagation in a windy, absorptive medium.

Expanding the governing equations (Eqs. 4 and 5) in a 2D Cartesian coordinate system in terms of individual components yields the update equations for the pressure fluctuations:

$$\frac{\partial p_s}{\partial t} = -w_x \frac{\partial p_s}{\partial x} - \rho_0 c^2 \left(\frac{\partial v_x}{\partial x} + \frac{\partial v_z}{\partial z} \right), \quad (15)$$

and for particle velocities

$$\frac{\partial v_x}{\partial t} = -v_z \frac{\partial w_x}{\partial z} - w_x \frac{\partial v_x}{\partial x} + \frac{1}{\rho_o} \left(-\frac{\partial p_s}{\partial x} + \eta \left(\frac{\partial^2}{\partial x^2} + \frac{\partial^2}{\partial z^2} \right) v_x + \eta \frac{\partial^2 w_x}{\partial z^2} + \left(\frac{\eta}{3} + \xi \right) \left(\frac{\partial^2 v_x}{\partial x^2} + \frac{\partial^2 v_z}{\partial x \partial z} \right) + f_x \right), \quad (16)$$

$$\frac{\partial v_z}{\partial t} = -w_x \frac{\partial v_z}{\partial x} + \frac{1}{\rho_o} \left(-\frac{\partial p_s}{\partial z} + \eta \left(\frac{\partial^2}{\partial x^2} + \frac{\partial^2}{\partial z^2} \right) v_z + \left(\frac{\eta}{3} + \xi \right) \left(\frac{\partial^2 v_x}{\partial x \partial z} + \frac{\partial^2 v_z}{\partial z^2} \right) + f_z \right). \quad (17)$$

The solution method may be simplified when there is no wind and only pressure values are sought. In that case, the $\eta \nabla^2 \bar{v}$ and $(\xi + \eta/3) \nabla(\nabla \cdot \bar{v})$ terms can be combined as $(\xi + 4\eta/3) \nabla^2 \bar{v}$ in the particle velocity equations. This would yield slight inaccuracies in the particle velocities but the computed pressures would remain accurate because the action of the divergence operator in the pressure equation (Eq. 4) on the attenuation terms yields

$\nabla \cdot [\eta \nabla^2 \bar{v} + (\xi + \eta/3) \nabla(\nabla \cdot \bar{v})] = (\xi + 4\eta/3) \nabla^2(\nabla \cdot \bar{v})$. This would be justified if only the pressure were of interest rather than particle velocity.

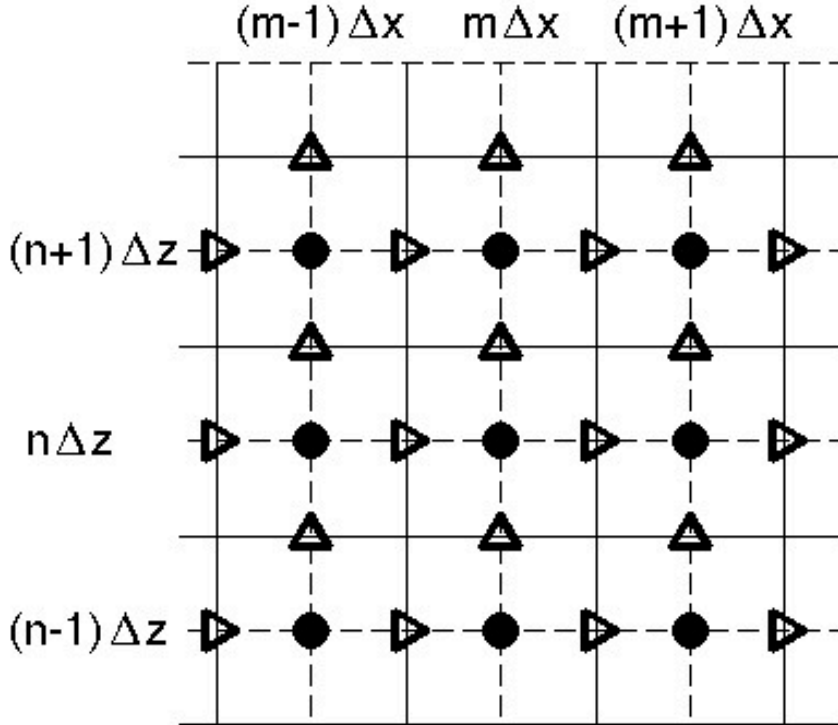


Figure 2. The finite difference model is decomposed into a set of discrete cells, indicated by the solid lines, each with uniform static sound speed c and ambient density ρ_o . The acoustic pressure and density perturbations are defined at the nodes at the center of each cell, indicated by the filled circles. The horizontal particle velocity v_x (triangles pointing right) and vertical particle velocity variables v_z (triangles pointing up) nodes straddle the cell boundaries of the spatially staggered grid, shown in two dimensions.

Equations 15-17 differ from those for a static atmosphere by the introduction of the advection terms involving $w_x \partial / \partial x$ and the wind shear term $v_z \partial w_x / \partial z$ in Eq. 16. Several numerical implementations have been suggested for the computation of the FDTD equations for sound propagation in windy environments (Blumrich & Heinmann 2002; Van Renterghem & Botteldoren 2003; Ostashev *et al* 2005). In particular, it is noted that inclusion of wind velocities in the first order equations complicates the standard method of staggering the velocities and pressures in both space and time, since the advection terms in the update equations imply that the first order derivatives in space and time are computed simultaneously, rather than serially as in the usual FDTD approach. Here, we use the FDTD method introduced by Ostashev *et al* (2005) for computing acoustic waves advected through a windy atmosphere. They suggest the use of a “non-staggered leap-frog” scheme, in which one forms centered temporal finite differences over two time steps, rather than the single time step in the staggered leap-frog approach (Yee 1966).

To explain the use of this FDTD scheme, we adopt the notation

$$P_{m,n}^j = p_s(m\Delta x, n\Delta z, j\Delta t), \quad (18a)$$

$$v_{x_{m+1/2,n}}^j = v_x((m+1/2)\Delta x, n\Delta z, j\Delta t), \quad (18b)$$

and

$$v_{z_{m,n+1/2}}^j = v_z(m\Delta x, (n+1/2)\Delta z, j\Delta t). \quad (18c)$$

We assume a model that is temporally invariant and vertically stratified, so the wind, sound speed, and ambient density are represented as $w_n = w_x(n\Delta z)$, $c_n = c(n\Delta z)$, and $\rho_n = \rho_o(n\Delta z)$. Here, we have dropped the x subscript on the wind since only horizontal winds are considered. The s subscript on the pressure is dropped since there are no ambient pressure terms, and the o subscript on the density is dropped since there are no terms involving density fluctuations. Using this notation, the update equation for the pressure fluctuations becomes

$$\frac{P_{m,n}^{j+1} - P_{m,n}^{j-1}}{2\Delta t} = -\rho_n c_n^2 \left[\frac{v_{x_{m+1/2,n}}^j - v_{x_{m-1/2,n}}^j}{\Delta x} + \frac{v_{z_{m,n+1/2}}^j - v_{z_{m,n-1/2}}^j}{\Delta z} \right] - w_n \frac{P_{m+1,n}^j - P_{m-1,n}^j}{2\Delta x}. \quad (19)$$

This equation indicates that updating the pressure in time requires storing each pressure field variable over two time steps, rather than over a single time step as in the standard leap-frog approach. That is, the values of the particle velocities at the j^{th} time point and the pressures at the j^{th} and $(j-1)^{\text{th}}$ time points are used to find the pressure at time $j+1$. The motivation for this is that we retain the accuracy of central differences in the temporal differencing operator, making the algorithm accurate for high Mach numbers. For the same reason the spatial finite differences in the advection term is taken over two grid points to provide centered spatial differences.

Similarly, the equation for the horizontal particle velocity becomes

$$\begin{aligned}
\frac{v_{x_{m+1/2,n}}^{j+1} - v_{x_{m+1/2,n}}^{j-1}}{2\Delta t} &= -v_{z_{m\#n}}^j \left(\frac{w_{n+1} - w_n}{\Delta z} \right) - w_n \frac{v_{x_{m+3/2,n}}^j - v_{x_{m-1/2,n}}^j}{2\Delta x} - \frac{1}{\rho_n} \left(\frac{p_{m,n}^j - p_{m-1,n}^j}{\Delta x} + f_{x_{m+1/2,n}} \right) \\
&+ \left(\frac{4\eta}{3\rho_n} + \frac{\xi}{\rho_n} \right) \left(\frac{v_{x_{m+3/2,n}}^j - 2v_{x_{m+1/2,n}}^j + v_{x_{m-1/2,n}}^j}{(\Delta x)^2} \right) + \frac{\eta}{\rho_n} \left(\frac{v_{x_{m+1/2,n+1}}^j - 2v_{x_{m+1/2,n}}^j + v_{x_{m+1/2,n-1}}^j}{(\Delta z)^2} \right) \\
&+ \left(\frac{\eta}{3\rho_n} + \frac{\xi}{\rho_n} \right) \left(\frac{v_{z_{m+1,n+1/2}}^j - v_{z_{m+1,n-1/2}}^j - v_{z_{m,n+1/2}}^j + v_{z_{m,n-1/2}}^j}{\Delta x \Delta z} \right) + \frac{\eta}{\rho_n} \left(\frac{w_{n+1} - 2w_n + w_{n-1}}{(\Delta z)^2} \right),
\end{aligned} \tag{20}$$

and the equation for the vertical particle velocity is

$$\begin{aligned}
\frac{v_{z_{m,n+1/2}}^{j+1} - v_{z_{m,n+1/2}}^{j-1}}{2\Delta t} &= -w_{n+1/2} \frac{v_{z_{m+1,n+1/2}}^j - v_{z_{m-1,n+1/2}}^j}{2\Delta x} - \frac{1}{\rho_{n+1/2}} \left(\frac{p_{m,n+1}^j - p_{m,n}^j}{\Delta z} + f_{z_{m,n+1/2}} \right) \\
&+ \frac{\eta}{\rho_n} \left(\frac{v_{z_{m+1,n+1/2}}^j - 2v_{z_{m,n+1/2}}^j + v_{z_{m-1,n+1/2}}^j}{(\Delta x)^2} \right) + \left(\frac{4\eta}{3\rho_n} + \frac{\xi}{\rho_n} \right) \left(\frac{v_{z_{m,n+3/2}}^j - 2v_{z_{m,n+1/2}}^j + v_{z_{m,n-1/2}}^j}{(\Delta z)^2} \right) \\
&+ \left(\frac{\eta}{3\rho_n} + \frac{\xi}{\rho_n} \right) \left(\frac{v_{x_{m+1/2,n+1}}^j - v_{x_{m+1/2,n}}^j - v_{x_{m-1/2,n+1}}^j + v_{x_{m-1/2,n}}^j}{\Delta x \Delta z} \right)
\end{aligned} \tag{21}$$

where $f_{x_{m,n}}$ and $f_{z_{m,n}}$ are the horizontal and vertical forces, respectively, acting in the horizontal direction at location $m\Delta x, n\Delta z$. The term $v_{z_{m\#n}}^j$ denotes the average particle velocity at the location of the $v_{x_{m,n}}^j$ node. As in Ostashev *et al* (2005) it is derived from the average of the four closest vertical particle velocities surrounding the horizontal velocity (see Fig. 2). The term $\rho_{n+1/2}$ in Eq. 21 denotes the average ambient density in the cells above and below the node for v_z .

The perfectly matched boundary layer method (Berenger 1994) is used to absorb waveforms at vertical side boundaries. Equations 19-21 are used to march the solution out in time, and the time-dependent pressure fluctuations are saved at locations corresponding to receiver locations.

B. Numerical Accuracy

Solutions derived using FDTD methods are inexact because the discretized equations (Eqs. 19-21) are approximations to the continuous differential equations that they replace (Eqs. 4-5). The magnitude of the errors depends on the sampling rates in both the spatial and temporal grids. The errors are manifested as numerical dispersion and spurious attenuation or growth; these non-physical artifacts are inherent to all FDTD techniques (e.g. Taflove & Hagness 2000). Note that numerical dispersion is an error introduced by discretizing the governing equations, and is distinct from the dispersion discussed in section II, which is a physical phenomenon.

We compute the numerical dispersion for the coupled equations by considering a very simple homogeneous medium with uniform density, sound speed, wind speed and viscosity. We know that the analytic solution is a wave equation of the form $e^{i(\vec{k} \cdot \vec{r} - \omega t)}$. Thus we may postulate solutions of the form

$$P_{m,n}^j = P_0 e^{i(\omega j \Delta t - \tilde{k}_x m \Delta x - \tilde{k}_z n \Delta z)}, \quad (22a)$$

$$v_{x_{m+1/2,n}}^j = V_{x_0} e^{i(\omega j \Delta t - \tilde{k}_x (m+1/2) \Delta x - \tilde{k}_z n \Delta z)}, \quad (22b)$$

and

$$v_{z_{m,n+1/2}}^j = V_{z_0} e^{i(\omega j \Delta t - \tilde{k}_x m \Delta x - \tilde{k}_z (n+1/2) \Delta z)}, \quad (22c)$$

where \tilde{k}_x and \tilde{k}_z are the finite difference approximations to the exact horizontal and vertical wavenumbers. The numerical approximations to the wavenumber differ from the true value of \tilde{k} by an amount that depends on the node spacing, the temporal resolution, as well as the frequency, the sound and wind speeds, and the direction of propagation.

Substituting Eq. 22a into the finite difference operator for $\partial p / \partial t$ in Eq. 19 leads to

$$\frac{P_{m,n}^{j+1} - P_{m,n}^{j-1}}{2\Delta t} = P_0 \frac{e^{i\omega\Delta t} - e^{-i\omega\Delta t}}{2\Delta t} e^{i(\omega j \Delta t - \tilde{k}_x m \Delta x - \tilde{k}_z n \Delta z)} = P_0 \frac{i \sin(\omega t)}{\Delta t} e^{i(\omega j \Delta t - \tilde{k}_x m \Delta x - \tilde{k}_z n \Delta z)} \quad (23)$$

using Euler's formula. We adopt the following notation

$$S_t = \sin(\omega\Delta t) / \Delta t; \quad S_x = 2 \sin(\tilde{k}_x \Delta x / 2) / \Delta x; \quad S_z = 2 \sin(\tilde{k}_z \Delta z / 2) / \Delta z; \quad S_w = \sin(\tilde{k}_x \Delta x) / \Delta x. \quad (24)$$

These values all approach 1 in the limit of small Δx , Δz , and Δt . Applying the substitutions Eqs. 22 to Eqs 19-21 leads to

$$S_t P_0 = \rho_o c^2 (S_x V_{x_0} + S_z V_{z_0}) + w S_w P_0, \quad (25)$$

$$S_t V_{x_0} = w S_w V_{x_0} + \frac{1}{\rho_o} S_x P_0 + i \left(\frac{4\eta}{3\rho_o} + \frac{\xi}{\rho_o} \right) S_x^2 V_{x_0} + i \frac{\eta}{\rho_o} S_z^2 V_{x_0} + i \left(\frac{\eta}{3\rho_o} + \frac{\xi}{\rho_o} \right) S_x S_z V_{z_0}, \quad (26)$$

$$S_t V_{z_0} = w S_w V_{z_0} + \frac{1}{\rho_o} S_z P_0 + i \frac{\eta}{\rho_o} S_x^2 V_{z_0} + i \left(\frac{4\eta}{3\rho_o} + \frac{\xi}{\rho_o} \right) S_z^2 V_{z_0} + i \left(\frac{\eta}{3\rho_o} + \frac{\xi}{\rho_o} \right) S_x S_z V_{x_0}. \quad (27)$$

The numerical dispersion relation is derived by combining Eqs. 25-27 to arrive at

$$(S_t - w S_w) [S_t - w S_w - i \left(\frac{4\eta}{3\rho_o} + \frac{\xi}{\rho_o} \right) (S_x^2 + S_z^2)] = c^2 (S_x^2 + S_z^2) \quad (28)$$

for a homogeneous, absorptive medium with uniform wind. Finally, we use square cells within the model grid, so that $\Delta x = \Delta z = \Delta$, so $\tilde{k}_x \Delta x = \tilde{k} \cos \theta \cdot \Delta$ and $\tilde{k}_z \Delta z = \tilde{k} \sin \theta \cdot \Delta$, where θ is the propagation angle with respect to the x -axis. Equation (28) then indicates that the numerical errors are a function of the propagation direction as well as the temporal and spatial sampling rates.

The grid and time sampling rates in an FDTD simulation depend on the highest frequencies used for propagation modeling. However, the finite difference propagation equations do not lead to a closed form expression for a stability limit on Δt when winds and attenuation are included. Instead we rely on modifying the Courant stability limit derived for a time-staggered algorithm for a viscosity-free, windless model ($\Delta t = \Delta / c$) for a guideline in choosing the time sampling rate. Our "non-staggered leap-frog" approach in which centered differences are formed over two time steps requires halving the sampling rate, and the inclusion of wind suggests that Δt be further reduced to account for the change in wavelength due to

advection. This suggests a maximum time sampling rate of $\Delta t = \Delta/[2(c+w)]$. For example, we consider a model with sound speed $c = 350$ m/s and a wind speed of $+50$ m/s in the $+x$ direction, and a source with upper frequency 0.5 Hz. A node spacing of 60 m results in sampling the waveform at 10 points in the direction of negative wind velocity at the upper end of the source bandwidth. The corresponding maximum time sampling rate would be 0.075 s; for greater accuracy, we chose a time discretization of 0.0375 s. We use the secant method to solve Eq. 28 for the values of \tilde{k} as a function of propagation angle, where the angle is defined positive anti-clockwise with respect to the $+x$ axis.

Figure 3a shows the normalized numerical sound speed $\tilde{c}/c = \omega_{\max}/\text{Re}(\tilde{k})$ as a function of propagation angle at the maximum source frequency for models with $\eta = \zeta = 1.8 \times 10^{-5} \text{ kg m}^{-1} \text{ s}^{-1}$ at a density $\rho_o = 1 \times 10^{-7} \text{ kg/m}^3$, equivalent to an altitude of about 110 km. These values, shown as dots, are superimposed on the values for numerical errors computed without attenuation. It is notable that the numerical sound speed is minimally affected by the attenuation. The figure indicates that numerical inaccuracies is a maximum for propagation directly upward (or downward) however, the total difference is less than 2% for the given discretization values. Figure 3b shows the normalized attenuation factors as a function of propagation angle, again indicating that the FDTD technique is the least accurate in a direction perpendicular to the wind, with the attenuation over-estimated by as much as 6% .

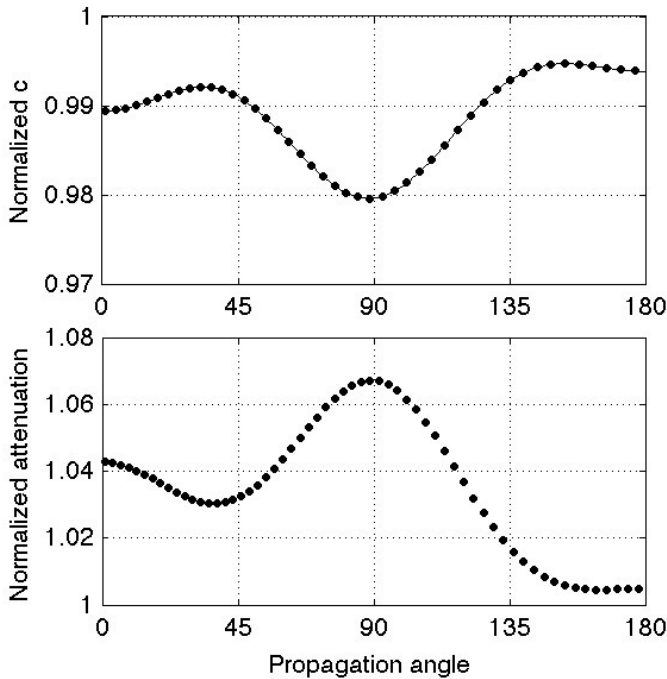


Figure 3. Numerical errors in the FDTD algorithm as a function of propagation angle for a model with $c=350$ m/s, $w=50$ m/s in the $+x$ direction, at a frequency of 0.5 Hz. Propagation angle is anti-clockwise with respect to the $+x$ axis. a) Variation of the normalized sound speed ratio \tilde{c}/c . The solid line are the values computed for a model with no attenuation. The dots indicate values computed for $\eta = \zeta = 1.8 \times 10^{-5} \text{ kg m}^{-1} \text{ s}^{-1}$ at a density $\rho_o = 1 \times 10^{-7} \text{ kg/m}^3$. b) Variation in attenuation ratios $\text{Im}(\tilde{k})/\text{Im}(k)$ for a model with attenuation as in a).

The results of Figure 3 only show the numerical errors introduced by the FDTD method at the very highest frequencies considered in the propagation; accuracy is greater at the lower frequencies. Figure 4 shows the normalized numerical sound speeds and dispersion values as a function of frequency for the same parameters and discretizations considered above, but this time for frequencies from 0 Hz to 0.5 Hz. The normalized sound speed and attenuation values are computed for a propagation angle of 0 degrees, i.e., for propagation in the $+x$ direction. As indicated, the numerical errors increase as a function of frequency, but errors in the normalized sound speed remain small, on the order of 1%, up to the maximum source frequency of 0.5 Hz considered for this example. Errors in attenuation also increase as a function of frequency and reach 6% at the upper source frequency. However, we consider this acceptable given that atmospheric attenuation values are not known precisely. Note that, since attenuation increases with increasing frequency, this formulation is more stable than that of de Groot-Hedlin (2008), where attenuation decreased with increasing frequency.

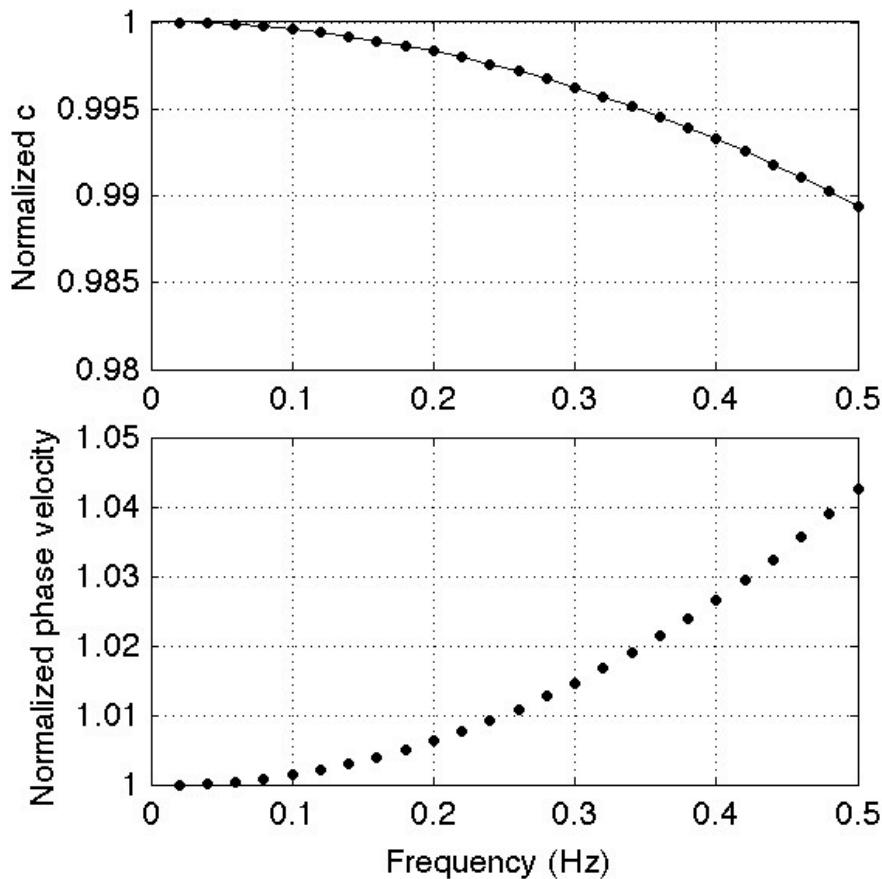


Figure 4. Numerical errors in the FDTD algorithm as a function of frequency for a model as in Fig. 3, computed at a propagation angle of 0 degrees. a) Variation of the normalized sound speed ratio \tilde{c}/c . The solid line are the values computed for a model with no attenuation. The dots indicate values computed for $\eta = \zeta = 1.8 \times 10^{-5} \text{ kg m}^{-1} \text{ s}^{-1}$ at a density $\rho_o = 1 \times 10^{-7} \text{ kg/m}^3$. b) Variation in attenuation ratios $\text{Im}(\tilde{k})/\text{Im}(k)$ for a model with attenuation as in a).

IV. APPLICATION TO BOLIDE

A. Bolide explosion

A bolide was observed before dawn on 19 February 2008 above northwestern states in the continental United States and western provinces of Canada. The source time and location of this event were determined with unusually high precision using data from seismic networks, global infrasound arrays, and video observations (Walker *et al* 2010). Specifically, acoustic-to-seismic coupled signals from the event registered clearly at several hundred seismic stations in regional networks and in the USArray Transportable Array. The close agreement between the seismic location and time of the event and the video location and time of the terminal burst indicates that the seismic signals were not due to sound shed from the hypersonic object as it passed through the atmosphere but from its terminal burst.

Because the location and time of the bolide explosion could be determined so precisely using the acoustic-to-seismic coupled signals, and because the source was impulsive, Hedlin *et al.* (2010) used the event to model the infrasound propagation out to a range of 500 km. Specifically, they picked the rise times for the different phases, an approach that is not impacted significantly by complications that arise from site-to-site variations in acoustic-to-seismic transmission characteristics. Atmospheric ray tracing was performed to predict travel times in a fully range-dependent, three-dimensional environment. The wind and sound speeds were derived from European Centre for Medium-Range Weather Forecasts (ECMWF) analysis products (Persson and Grazzini, 2007) up to an altitude of 75 km and the HWM07/MSISE-00 empirical climatologies (Drob *et al* 2008; Picone *et al* 2002) above 75 km. They found that most arrivals were either tropospheric or stratospheric in origin. However, a cluster of late arrivals to the southwest of the bolide explosion was associated with refraction in the thermosphere.

In this section, we examine arrivals along a single azimuth and perform ray tracing to identify expected travel paths, travel times, and expected frequency content for simplified one-dimensional sound and wind speed profiles. We then use the FDTD method described above to synthesize a cluster of late arrivals at stations to the southwest of the source, at ranges over 250 km, identified by ray tracing as being associated with refraction in the lower thermosphere (Hedlin *et al* 2010).

B. Preliminary modeling using ray tracing

For the time period of interest to this study, noise levels at USArray seismic stations peaked at about 0.2 Hz, roughly the peak of the microbarometric spectrum; at this frequency, noise levels were approximately four orders of magnitude greater than between 2-8 Hz. Infrasound signals were not observed at frequencies below 1 Hz, almost certainly because noise levels were too high. Figure 5 shows 2-8 Hz bandpassed waveforms recorded at seismic stations along an azimuth of 210° , for ranges up to nearly 350 km from the source. A reducing velocity of 400 m/s was used to allow us to display the signals more clearly. To illustrate infrasound propagation along this azimuth, ray paths were re-computed for simplified atmospheric sound and wind profiles using a tau-p method developed for an advected medium (Garcés *et al* 1998). We used identical wind and sound speed profiles for the ray and FDTD computations in order to provide a direct comparison of results. Since deviation of the infrasound travel path out of the source-receiver plane cannot be considered for the 2D FDTD computations, we neglected cross-

wind components in our model. Furthermore, examination of the ECMWF analysis products and HWM07/MSISE-00 empirical climatologies for this event indicated that there was little variation in wind and sound speeds along path to a range of 350 km from the source; with mean along path variations of 0.6 m/s in sound speed and 1.8 m/s in wind speeds at each altitude. Consequently, atmospheric wind and sound speeds were represented by range-independent values that were derived by averaging the sound and wind profiles along this azimuth. The average sound speed profile was shown in Figure 1b as the static sound speed profile; the average wind speed profile along the path is shown in Figure 6.

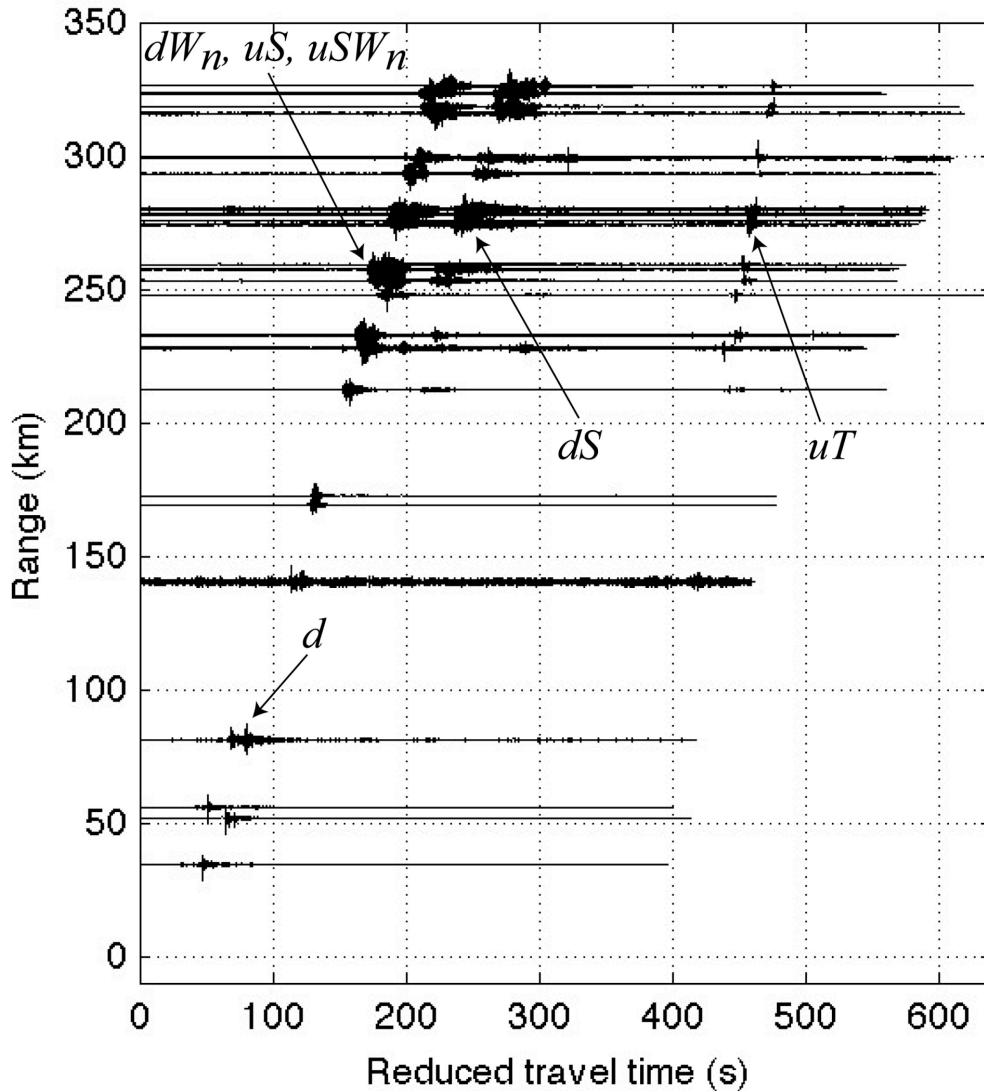


Figure 5. Seismic velocity responses, bandpassed from 2-8 Hz, along a profile from 210 degrees with respect to north. Ranges are with respect to the source location. The time scale has been reduced by 400m/s. The traces have been scaled such that each waveform has the same peak amplitude. Arrivals are labeled using the nomenclature of Hedlin *et al* (2010).

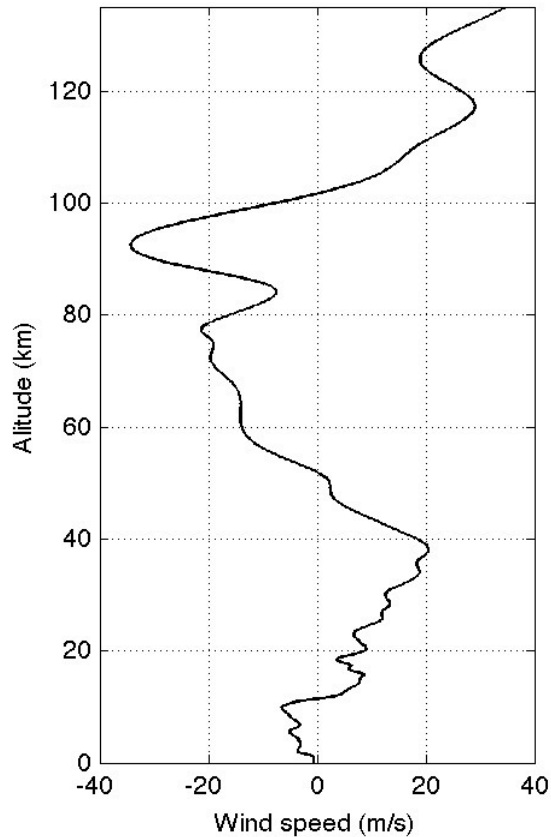


Figure 6. Average wind speed profile for 1400 UT, Feb 19 2008, along a 350 km path at an azimuth of 210° from north, beginning at the location of the bolide explosion. Static sound speeds were shown in Figure 1b.

Figure 7a shows computed ray paths for propagation along this azimuth. For these computations, the Earth's surface was represented by a rigid, flat boundary at an elevation of 1450 m, the average elevation above sea level at this azimuth. Rays were calculated up to a maximum altitude of 123 km, and only rays that reach the ground are shown. Rays turning above this altitude were excluded from this study due to the predicted high attenuation. Ray tracing shows that the first arrivals at each station either propagated directly downward from the source (branch d , using the nomenclature of Hedlin et al 2010), or were then tropospherically ducted (dWn ; predicted at ranges beyond 100 km). Beyond about 150 km, these arrivals merge with a branch of acoustic energy that initially propagated upward from the terminal burst and was then refracted back to the Earth within the stratosphere (branch uS) with additional arrivals at greater ranges predicted due to ducting in the troposphere (branch $uSWn$). The second arrivals, observed at distances starting about 250 km, result from acoustic energy that is stratospherically ducted after first propagating down from the source and reflecting from the Earth's surface (branch dS). The third set of arrivals, beyond 225 km from the source and about 4 minutes after the first arrivals, are thermospherically ducted after being directed up from the source (uT). The final set of arrivals in the ray diagram is identified with infrasound energy that

is thermospherically ducted after first propagating down from the source and reflecting from the Earth's surface (branch dT). Note that the arrival pattern shown in Figure 7b is a reasonably close match to the real data (Figure 5), with the exception of the final branch dT , which is not observed in the waveform data.

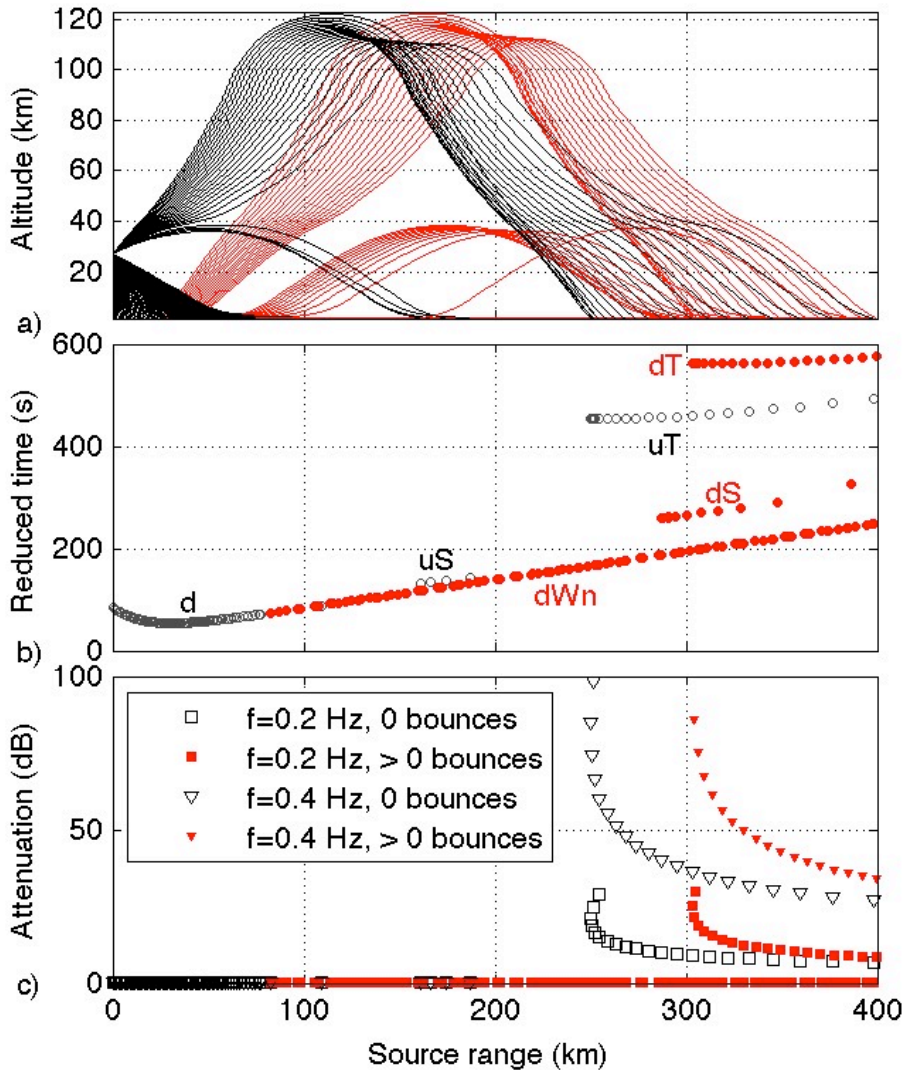


Figure 7. a) Ray diagram, showing rays that reach the ground. Black lines indicate rays that have not undergone reflection at the surface. Rays that have undergone at least one bounce are shown in red. A flat ground surface has been used to compute ray paths, so that rays do not steepen or become shallower as they bounce along the surface. b) Corresponding arrival times, reduced by 400 m/s. Arrivals are labeled using the nomenclature of Hedlin *et al* (2010). c) Corresponding attenuation values, at $f = 0.2$ Hz and $f = 0.4$ Hz, computed for a viscosity coefficient of $\eta = 1.8 \times 10^{-5} \text{ kg m}^{-1} \text{ s}^{-1}$ and bulk viscosity $\zeta = 0.6\eta$. Significant attenuation is predicted only for thermospheric rays.

We use ray tracing to obtain a first order estimate of the attenuation for a given ray path. Given the computed ray path, and the equation for the attenuation due to viscosity as a function of density, sound speed, and frequency (Eq. 12, and see Fig 1c), approximate attenuation values for each path can be computed by integrating the absorption values along segments of each raypath. The total attenuation along each raypath is shown in Fig 7c for 0.2 Hz and 0.4 Hz. As indicated, infrasound propagating in the troposphere and stratosphere undergoes negligible attenuation at these frequencies, while thermospheric returns undergo significant absorption. Rays that propagate higher than 120 km altitude are even more highly attenuated. Note that attenuation estimates based on ray results do not yield relative amplitudes between tropospheric, stratospheric and thermospheric returns, since these results do not take relative ray densities into account. Figure 1 indicates that there is no significant physical dispersion at these frequencies.

C. FDTD simulation of low frequency infrasound propagation

The ray path analysis suggests that thermospheric returns undergo substantial attenuation at frequencies above at least 0.2 Hz; as indicated in Figure 7c, infrasound undergoes about 6 dB attenuation at 0.2 Hz, i.e. the amplitudes are halved; at 0.4 Hz, the attenuation is about 30 dB and amplitudes are reduced by approximately a factor of 30. Thus, we used a source term with a maximum frequency of 0.45 Hz in our FDTD simulation of low frequency infrasound propagation from the bolide terminal burst to compare the differences in predicted absorption between tropospheric/stratospheric and thermospheric paths. We do not consider higher frequencies because of limited computational resources. The bolide explosion is represented temporally as a Gaussian pulse and spatially as a point at 27 km altitude; the source is modeled as an external force added to the particle velocity terms, as in Equation 2.

The waveforms in Figure 5 show the vertical seismic velocity responses, so in the FDTD simulation we model the vertical particle velocities v_z , which were sampled every 10 km along the ground to a range of 340 km. Unless otherwise stated, the ground was modeled as a flat boundary at an elevation of 1.45 km, equal to the average elevation along a transect 210° from the bolide terminal burst. The top of the model was set to 123 km altitude. Given the sound and wind speed profiles displayed in Figures 1b and 6, and the maximum source frequency of 0.45 Hz, a node spacing of 50 m was chosen. For the lowest sound and wind speeds (and upper source frequency), this yields a node spacing of 11 nodes per wavelength.

The FDTD synthesis was run four times: (1) with attenuation using a viscosity coefficient of $\eta = 1.8 \times 10^{-5} \text{ kg m}^{-1} \text{ s}^{-1}$ and bulk viscosity $\zeta = 0.6\eta$, (2) with no attenuation, (3) with the Earth's surface lowered to an elevation of 0 km, and (4) with realistic topography included, where elevations were taken from the ETOPO1 global relief model (Amante & Eakins 2009). For the runs where attenuation was included, the time sampling rate was set to 0.0287 s, equivalent to a Courant stability factor of $1/4$. For the run where attenuation was neglected, the time sampling rate was set to 0.0382 s, equivalent to a Courant stability factor of $1/3$.

Figure 8 shows the result of the FDTD synthesis run with attenuation, with viscosity $\eta = 1.8 \times 10^{-5} \text{ kg m}^{-1} \text{ s}^{-1}$ and bulk viscosity $\zeta = 0.6\eta$. For comparison, Figure 9 shows the equivalent results for the FDTD computations without attenuation. Both FDTD simulations show that the dS arrivals, those that are refracted in the stratosphere after reflection at the Earth's surface appear at ranges of nearly 250 km from the source, in agreement with the data. Furthermore, the first thermospheric arrivals appear at approximately the same range, and at times that provide a close fit to the data. However, the main difference between the waveforms of Figures 8 and 9 is

in the late arrivals associated with refraction in the thermosphere. The amplitudes of the late arrivals in Figure 8, computed with non-zero viscosity, are lower than those of Figure 9; the higher frequencies have been preferentially attenuated in Figure 8 as expected.

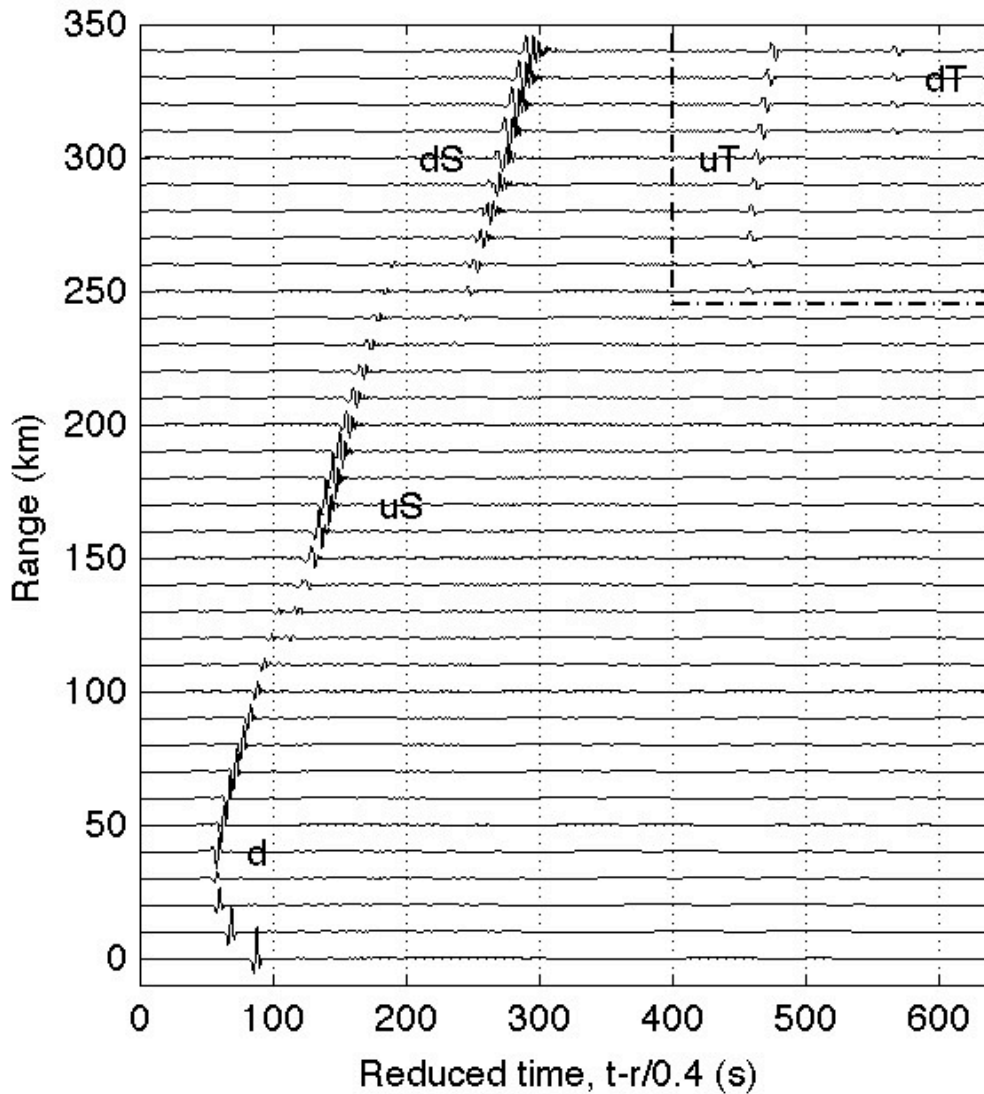


Figure 8. FDTD synthesized v_z waveforms for stations at 10 km intervals from a source at 27 km altitude. This shows the results of simulation 1: the FDTD algorithm was run with a viscosity coefficient of $\eta = 1.8 \times 10^{-5} \text{ kg m}^{-1} \text{ s}^{-1}$ and bulk viscosity $\zeta = 0.6\eta$, and the ground was modeled as a flat surface at an elevation of 1.45 km, the average elevation along a 210° azimuth from the Oregon bolide. Each waveform is scaled by multiplying by the square root of the distance between the source and receiver to correct approximately for geometric spreading. The thermospheric arrivals in the dash-dotted box at top right are examined in greater detail in Figure 10.

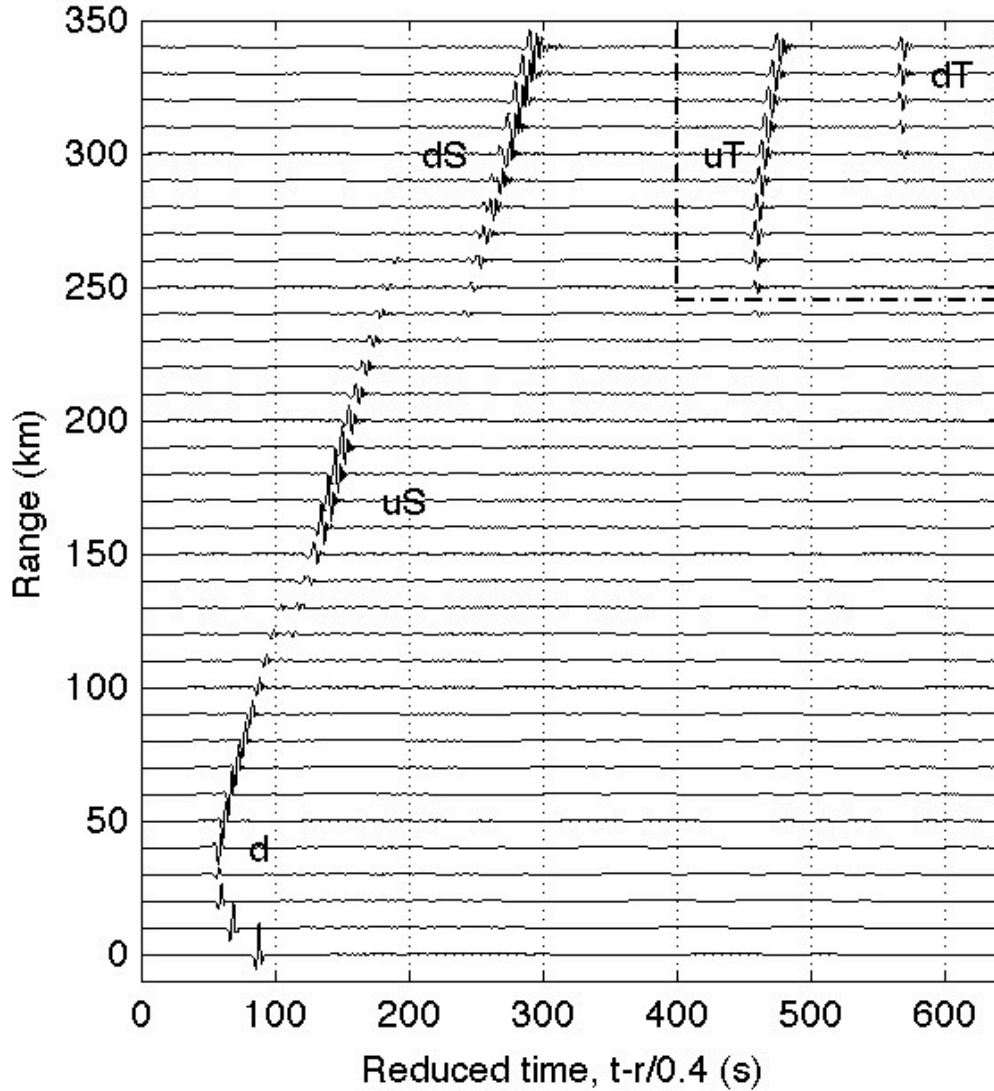


Figure 9. As for Figure 8, except that that in this simulation, the viscosities $\eta = \zeta = 0$.

We examine the amplitude and frequency differences in greater detail in Figure 10, which shows the late arrivals for both FDTD runs and the corresponding amplitude spectra at ranges over 225 km from the source. The amplitudes of the attenuated arrivals (Fig 10a, red lines) are lower than those of the corresponding arrivals for the FDTD synthesis without attenuation (blue lines). The corresponding average amplitude spectral ratios (Fig 10b) were computed for reduced arrival times between 400 – 540 s, i.e. the first thermospheric arrivals, at ranges from 250 to 340 km from the source. The spectra indicate that increasing attenuation with increasing frequency above 0.1 Hz occurs within the thermosphere when atmospheric viscosity is included in the propagation modeling. These results are in agreement with the attenuation values estimated for this range from the ray analysis (Figure 5b). The increasing absorption with increasing frequencies implies that, had higher frequencies been modeled, infrasound energy refracted within the thermosphere would be so severely attenuated that it

would be undetectable. Thus there is a discrepancy between our modeling results and the data, which clearly show infrasound energy at frequencies above 2 Hz. We address this further in the next section.

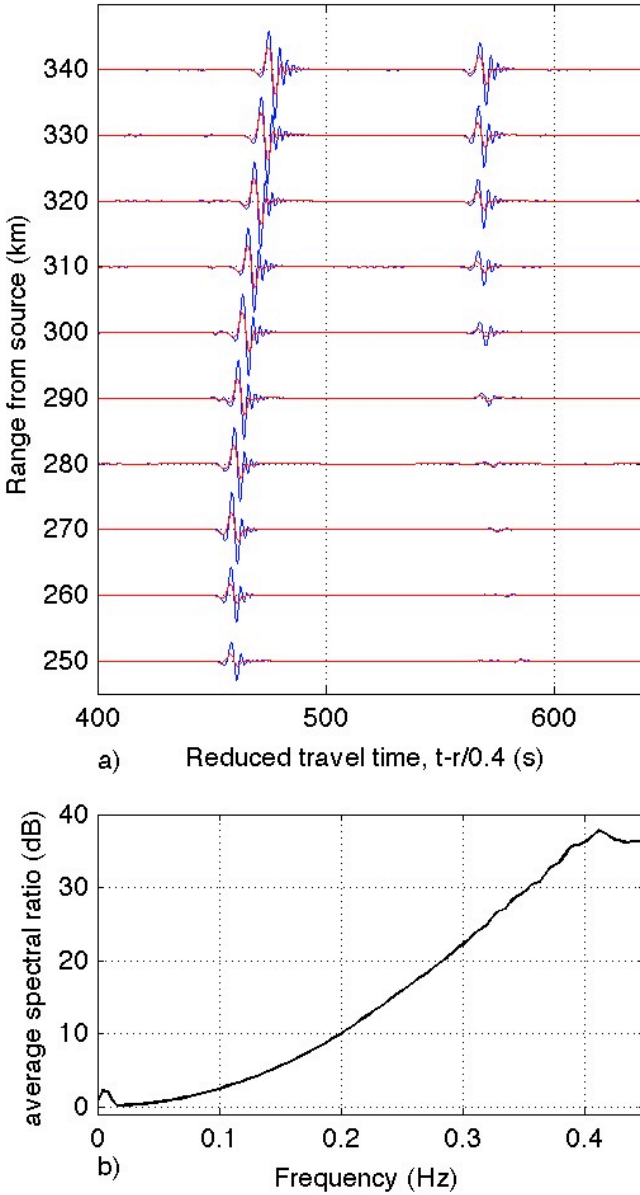


Figure 10. Comparison of thermospheric arrivals. a) Late arrivals associated with refraction in the thermosphere. The blue lines are the vertical particle motions for the model run with no attenuation, the red lines are the corresponding waveforms for a viscosity coefficient of $\eta = 1.8 \times 10^{-5} \text{ kg m}^{-1} \text{ s}^{-1}$ and bulk viscosity $\zeta = 0.6\eta$. b) Average spectral ratios of non-attenuated vs. attenuated waveforms for reduced times $400 \text{ s} < t_{\text{red}} < 540 \text{ s}$, in dB, at ranges from 250 to 340 km from the source.

A major difference between the observed waveforms and the FDTD waveforms is the absence of tropospherically ducted energy (dWn and $uSWn$) in the FDTD results (Figures 8 and 9), which show up in the observed waveforms as the first arrivals at all ranges (Figure 5). Using the ETOPO1 global topography model with a 1.9 km x/y spatial resolution (Amante & Eakins, 2009), we re-computed the FDTD waveforms to examine whether the inclusion of topography would explain the observed tropospheric ducting. It did not. We again re-computed the waveforms after altering the model such that the surface was at an elevation of 0 km to examine the effect of a thicker surface duct on the first arrivals. In this case, the synthesized waveforms did indeed result in tropospheric ducting of infrasound energy. We attribute this to the fact that a thicker duct can accommodate lower frequencies than a narrow one; low frequencies are stripped away by a narrow duct (Negraru & Herrin, 2009). However, higher frequencies can be trapped within a narrow duct. Thus, this discrepancy between modeled and observed waveforms does not require inaccuracies in the sound and wind speed models, or in the FDTD algorithm. Instead, it may be explained by the fact that we are using a higher frequency band for the observed waveforms for visualization purposes (Figure 5), and these higher frequencies (relative to the lower frequencies in the FDTD model) can be trapped in the narrow duct near the Earth's surface.

V. DISCUSSION

The large bolide of 2008 that burst above the USArray transportable array, and other dense regional networks in the US Pacific Northwest, provided an opportunity to examine acoustic branches from an impulsive source to several hundred km from the source (Hedlin et al 2010). In this paper we have taken the next step in this analysis by developing a finite difference time domain code that incorporates winds, attenuation and atmospheric heterogeneity to model propagation from this source and to compare the synthetics with the recorded data.

The first observation from this comparison (observed data in Figure 5 versus synthetic data in Figure 8) is that the first arrivals do not agree very well at ranges beyond about 100 km. Ray theory predicts that these branches result from the ducting of energy in a narrow duct near the surface. However, the entrainment of energy in a narrow duct is frequency-dependent, a phenomenon that is not described by ray physics. Acoustic energy with wavelengths greater than the width of the duct is not trapped, while energy at shorter wavelengths (higher frequencies) can be trapped. Thus these differences reflect the fact that the near surface duct is very thin, and that we are comparing high frequency recorded data to lower frequency synthetics. Unfortunately, the high noise levels observed at low frequencies at the USArray stations preclude a direct comparison of observed versus synthetic data at lower frequencies.

However, our primary interest is in comparing thermospherically ducted infrasound energy. As discussed in Hedlin et al (2010) the two main thermospheric paths from this event are dT , energy down from the bolide and ducted through the thermosphere after a single reflection from the Earth's surface and uT , a simple propagation path up from the source and ducted in the thermosphere. We note that the seismic network recordings from stations at an azimuth of 210 degrees with respect to north show a thermospheric branch of signals (uT) arriving at about the same time and at the same ranges as predicted by both rays and FDTD computations. This validates the sound and wind velocity models used in this study.

Although the time and range extent of the uT branch agree well, a significant difference between the observed and synthetic waveforms is in the relative frequency content. FDTD computations show that energy refracted in the thermosphere undergoes significant attenuation at frequencies above 0.1 Hz. This is in agreement with our method of integrating predicted infrasound propagation along raypaths (Figure 7b). However, the data show that there is relatively more high frequency energy in the thermospheric arrivals than the predictions would suggest. Figure 5 shows that there is significant energy in the thermospherically refracted infrasound signals in the band from 2 to 8 Hz. Our predictions of attenuation, both from raypaths and from FDTD synthesis, indicate that thermospherically ducted arrivals would have insignificant amplitude at these frequencies. We propose three possible hypotheses:

- 1) The upper altitude sound speed profiles are incorrect and late arriving energy actually is refracted back to the ground from the lower thermosphere where attenuation is much less severe. This is contradicted by the fact that the observed thermospheric arrivals agree quite well with the predicted arrival times and ranges. The agreement of the timing of the synthetic and recorded branches suggests that sound and wind speed profiles are acceptable, so we discard this hypothesis.
- 2) Attenuation within the thermosphere is significantly lower than expected, i.e. lower than estimates provided by Sutherland and Bass (2004). This implies either that the viscosity coefficient, which has a value on the order of $\eta = 1.8 \times 10^{-5} \text{ kg m}^{-1} \text{ s}^{-1}$ up to elevations of 86 km (Gill, 1982), decreases significantly at higher elevations, or that the assumption that the atmosphere behaves as a Newtonian fluid is incorrect. This latter assumption was implicit in applying the Navier-Stokes equation (Equation 2) to describe acoustic propagation in a viscous medium. It is possible that infrasound propagation is significantly altered by changes in atmospheric composition with altitude, or that the atmosphere is increasingly ionized at altitudes above about 90 km. In this case, the Sutherland-Bass attenuation model would need improvements to incorporate these effects.
- 3) Some wavefront steepening occurs as energy propagates to very high altitudes where the ambient pressure is extremely low. At these altitudes the linear assumptions – that the pressure of the sound wave is negligible compared to the ambient pressure and that particle velocities are much lower than the ambient sound speed – may be incorrect. If this is so, non-linear propagation would cause some re-population of high frequencies. If non-linear effects are indeed significant within the thermosphere the simple linear algorithm used here is insufficient. In this case, a numerical synthesis method incorporating non-linear effects within the upper atmosphere would have to be developed in order to accurately model infrasound propagation within the atmosphere.

This paper introduces two tools with which to test infrasound propagation physics hypotheses by comparing observations to numerical models. We anticipate that waveform modeling methods of this type may be used to place more accurate limits on wind speeds and acoustic attenuation within the thermosphere and provide tighter constraints on high amplitude sources, both explosions and large volcanic eruptions.

The application of these tools to the study of the Oregon bolide underscores the value of densely sampled infrasound data for atmospheric modelling studies. Although the global infrasound network provides more coverage of the infrasound wavefield than we have ever had

before, the network is still very sparse. The infrasound arrays offer precise spot measurements of the true infrasound wavefield, but do not reveal the details of how signals vary with range and azimuth from the source because the average distance between infrasound arrays in the global IMS network is $\sim 3,000$ km. With the spatial coverage provided by dense seismic networks, we can map out variations in the infrasound wavefield our test hypotheses governing these arrival patterns with such modeling codes.

VI. CONCLUSIONS

We have presented the equations relevant to infrasound propagation within a windy medium in which viscosity is the dominant absorption mechanism. The equations do not account for infrasound absorption due to thermal losses or molecular vibration losses, which dominate at lower altitudes but remain negligible at infrasound frequencies. An analytic solution was derived for a windless medium with constant density and sound speed, which yields equations for the frequency dependent phase speeds and attenuation values. These equations are applicable to media with densities and sound speeds that vary at scale lengths much greater than the infrasound wavelength. We assumed that the viscosity coefficient within the thermosphere was approximately equal to its value below 86 km; this estimate results in total attenuation values within the thermosphere that are in close agreement with those derived in Sutherland and Bass (2004) at infrasound frequencies. Under this assumption, we showed that infrasound dispersion is insignificant at altitudes below 120 km at frequencies below 2 Hz, and that attenuation is approximately proportional to the square of the frequency.

We discretized the equations for linear acoustic propagation through an absorptive, heterogeneous, windy atmosphere to develop a FDTD method of synthesizing infrasound waveforms. We describe an FDTD method that is spatially staggered, but centered temporal finite differences are formed over two time steps, as in Ostashev *et al* (2005), to retain the accuracy of central differences through a windy atmosphere. Analysis of the numerical accuracy shows that the number of nodes required per wavelength is comparable to the number required for the case where attenuation is not included (e.g. Taflove & Hagness 2000); however, a smaller time step is required to retain accuracy. (Note that we could have used a higher order FDTD approach rather than the first order staggered grid used. In that case, eqs. 15-17 would be used as the starting point for further code development.)

Application of the FDTD synthetic modeling to real data shows its utility. We find that standard attenuation models (Sutherland-Bass) predict much greater attenuation within the thermosphere than is observed. We conclude that either the standard attenuation model for the thermosphere is incorrect, or that thermospheric returns are a result of non-linear propagation at very high altitude. In the former case, a better understanding of atmospheric absorption at high altitudes is required; in the latter case, a fully nonlinear numerical method is needed to test our hypothesis that higher frequency arrivals from the thermosphere result from nonlinear propagation at thermospheric altitudes.

Acknowledgements

The authors are grateful to Douglas Drob of the Naval Research Laboratory for providing the atmospheric specifications used in the propagation modeling, and to David Norris for his careful review. This publication was made possible through support provided by US Army Space and Missile Defense Command. The opinions expressed herein are those of the author(s) and do not necessarily reflect the views of the US Army Space and Missile Defense Command.

References

- Amante, C. & Eakins, B.W., 2009. *Etopo1 1 arc-minute global relief model: procedures, data sources, and analysis*, NOAA Technical Memorandum NESDIS NGDC-24, National Geophysical Data Center, Boulder, Colorado.
- Arrowsmith, S.J. & Hedlin, M.A.H., 2005. Observations of infrasound from surf in southern California, *Geophys. Res. Lett.*, 32, L09810, doi:10.1029/2005GL022761.
- Arrowsmith, S.J., Drob, D.P., Hedlin, M.A.H. & Edwards, W., 2007. A joint seismic and acoustic study of the Washington State bolide: Observations and modeling, *J. Geophys. Res.*, 112, D09304, doi:10.1029/2006JD008001.
- Bass, H.E., Bhattacharyya, J., Garcés, M.A., Hedlin, M., Olson, J.V. & Woodward, R.L., 2006. Infrasound, *Acoustics Today*, 2, 9-19.
- Bass, H.E., Hetzer, C.H., & Raspet, R., 2007, On the speed of sound in the atmosphere as a function of altitude and frequency, *J. Geophys. Res.*, 112, D15110, doi:10.1029/2006JD007806.
- Berenger, J.P., 1994. A perfectly matched layer for the absorption of electromagnetic waves, *Journal of Computational Physics*, 114, 185-200.
- Blumrich, R. & Heimann, D., 2002. A linearized Eulerian sound propagation model for studies of complex meteorological effects, *J. Acoust. Soc. Am.*, 112, 446-455.
- Ceranna, L., Le Pichon, A., Green, D.N. & Mialle, P., 2009. The Buncefield explosion: a benchmark for infrasound analysis across Central Europe, *Geophys. J. Int.*, 177, 491-508.
- Christie, D.R. & Campus, P., 2010. The IMS infrasound network: design and establishment of infrasound stations, in *Infrasound monitoring for atmospheric studies*, pp. 29–75, eds. Le Pichon, A., Blanc, E. & Hauchecorne, A., Springer.
- de Groot-Hedlin, C.D., Hedlin, M.A.H., Walker, K.T., Drob, D.D. & Zumberge, M.A., 2008. Evaluation of infrasound signals from the shuttle Atlantis using a large seismic network, *J. Acoust. Soc. Am.*, 124, 1442-1451.
- de Groot-Hedlin, C.D., 2008. Finite-difference time-domain synthesis of infrasound propagation through an absorbing atmosphere, *J. Acoust. Soc. Am.*, 124, 1430-1441.
- Donn W. & Rind D., 1971. Natural infrasound as an atmospheric probe, *Geophys. J. R Astron. Soc.*, 26, 111–133.
- Drob, D.P., Picone, J.M. & Garcés, M., 2003. Global morphology of infrasound propagation, *J. Geophys. Res.*, 108 (D21), 4680, doi:10.1029/2002JD003307.

- Drob, D.P., Emmert, J.T., Crowley, G., Picone, J.M., Shepherd, G.G., Skinner, W., Hays, P., Niciejewski, R.B., Larsen, M., She, C.Y., Meriwether, J.W., Hernandez, G., Jarvis, M.J., Sipler, D.P., Tepley, C.A., O'Brien, M.S., Bowman, J.R., Wu, Q., Murayama, Y., Kawamura, S.W., Reid, I.M. & Vincent, R.A., 2008. An empirical model of the Earth's horizontal wind fields: HWM07, *J. Geophys. Res.-Space Physics*, 113, doi:10.1029/2008JA013668.
- Edwards, W.N., 2010. Meteor generated infrasound: theory and observation, in *Infrasound monitoring for atmospheric studies*, pp. 355–408, eds. Le Pichon, A., Blanc, E. & Hauchecorne, A., Springer.
- Evers, L.G., & Haak, H.W., 2005. The detectability of infrasound in The Netherlands from the Italian volcano Mt. Etna, *J. Atmos. and Solar-Terr. Phys.*, 67, 259-268.
- Evers, L.G. & Haak, H.W., 2010. The Characteristics of Infrasound, its Propagation and Some Early History, in *Infrasound Monitoring for Atmospheric Studies*, pp. 3-26, eds. Le Pichon, A., Blanc, E. & Hauchecorne, A., Springer.
- Fee, D. & Garcés, M., 2007. Infrasonic tremor in the diffraction zone, *Geop. Res. Lett.*, 34, L16826, doi:10.1029/2007GL030616.
- Garcés, M., Hansen, R.A. & Lindquist, K.G., 1998. Travel times for infrasonic waves propagating in a stratified atmosphere, *Geop. J. Int.*, 135, 255-263.
- Garcés, M., Hetzer, C., Merrifield, M., Willis, M. & Aucan, J., 2003. Observations of surf infrasound in Hawai'i, *Geophys. Res. Lett.*, 30, 2264, doi:10.1029/2003GL018614.
- Gill, A.E., 1982. *Atmosphere-Ocean Dynamics*, Academic Press, San Diego, CA, USA.
- Gutenberg B., 1939. The velocity of sound waves and the temperature in the stratosphere in Southern California, *Bull. Seis. Soc. Am.*, 20, 192–201.
- Hedlin, M., Drob, D., Walker, K. & de Groot-Hedlin, C., 2010. A study of acoustic propagation from a large bolide in the atmosphere with a dense seismic network, *J. Geophys. Res.*, 115, B11312, doi:10.1029/2010JB007669.
- Hetzer C.H., Gilbert, K.E., Waxler, R. & Talmadge, C.L., 2010. Generation of microbaroms by deep ocean hurricanes, in *Contribution of a global continuous infrasound monitoring for atmospheric studies*, pp. 245–258, eds. Le Pichon, A., Blanc, E. & Hauchecorne, A., Springer.
- Jensen, F. B., Kuperman, W. A., Porter, M. B. & Schmidt, H., 1994. *Computational Ocean Acoustics* AIP, Woodbury, NY.
- Landau, L.D. & Lifshitz, E.M., 1959. *Fluid Mechanics*, 2nd edn, Elsevier, Burlington, MA.
- Le Pichon, A., Herry, P., Mialle, P., Vergoz, J., Brachet, N., Garcés, M., Drob, D. & Ceranna, L., 2005a. Infrasound associated with 2004-2005 large Sumatra earthquakes and tsunami, *Geop. Res. Lett.*, 32, L19802, doi:10.1029/2005GL023893.
- Le Pichon, A., Blanc, E., Drob, D., Lambotte, S., Dessa, J.X., Lardy, M., Bani, P. & S. Vergnoille, 2005b, Infrasound monitoring of volcanoes to probe high-altitude winds, *J. Geophys. Res.*, 110, D13106, doi:10.1029/2004JD005587.
- Le Pichon, A., Blanc, E. & Drob, D., 2005c. Probing high-altitude winds using infrasound, *J. Geophys. Res.*, 110, D20104, doi:10.1029/2005/D006020.
- Le Pichon, A., Mialle, P., Guilbert, J. & J. Vergoz, 2006. Multistation infrasonic observations

- of the Chilean earthquake of 2005 June 13, *Geophys. J. Int.*, 167, 838 – 844.
- Le Pichon, A., Vergoz, J., Blanc, E., Guilbert, J., Ceranna, L., Evers, L. & N. Brachet, 2009. Assessing the performance of the International Monitoring System's infrasound network: Geographical coverage and temporal variabilities, *J. Geophys. Res.*, 114, D08112, doi:10.1029/2008JD010907.
- Lighthill, J., 1978. *Waves in Fluids*, Cambridge Mathematical Library, Cambridge, UK.
- Lingevitch, J.F., Collins, M.D., Dacol, D.K., Drob, D.P., Rogers, J.C. & Seigmann, W.L., 2002. A high angle and high Mach number parabolic equation, *J. Acoust. Soc. Am.*, 111, 729-734.
- Lingevitch, J.F., Collins, M.D. & Siegmann, W.L., 1999. Parabolic equations for gravity and acousto-gravity waves, *J. Acoust. Soc. Am.*, 105, 3049-3056.
- Matoza, R.S., Hedlin, M.A.H. & Garcés, M.A., 2006. An infrasound array study of Mount St. Helens, *J. Volcanology and Geothermal Res.*, 160, 249-262, doi:10.1016/j.jvolgeores.2006.10.006.
- Matoza, R.S., Garcés, M.A., Chouet, B.A., D'Auria, L., Hedlin, M.A.H., de Groot-Hedlin, C. & Waite, G.P., 2009. The source of infrasound associated with long-period events at Mount St. Helens, *J. Geophys. Res.*, 114, B04305, doi:10.1029/2008JB006128.
- Negraru, P.T. & Herrin, E.T., 2009. On Infrasound Waveguides and Dispersion, *Seis. Res. Lett.*, 80, 565-571.
- Ostashev, V.E., Wilson, D.K., Liu, L., Aldridge, D.F., Symons, N.P. & Marlin, D., 2005. Equations for finite-difference, time-domain simulation of sound propagation in moving inhomogeneous media and numerical implementation, *J. Acoust. Soc. Am.*, 117, 503-517.
- Ottmøller, L. & L.G. Evers, 2008. Seismo-acoustic analysis of the Buncefiled oil depot explosion in the UK, 2005 December 11, *Geophys J. Int.*, 172, 1123-1134.
- Persson, A. & Grazzini, F., 2007. User Guide to ECMWF forecast products, ECMWF Meteorological Bulletin M3.2, <http://www.ecmwf.int/products/forecasts/guide>.
- Picone, J.M., Hedin, A.E., Drob, D.P. & Aikin, A.C., 2002. NRLMSISE-00 empirical model of the atmosphere: Statistical comparisons and scientific issues, *J. Geophys. Res.*, 107(A12), 1468, doi:10.1029/2002JA009430
- Revelle, D.O., Brown, P.G. & Spurny, P., 2004. Entry dynamics and acoustics/infrasonic/seismic analysis for the Neuschwanstein meteorite fall, *Meteoritics and Planetary Science*, 39, 1605–1626.
- Sutherland, L.C. & Bass, H.E., 2004. Atmospheric absorption in the atmosphere up to 160 km, *J. Acoust. Soc. Am.*, 115, 1012-1032.
- Taflove, A. & Hagness, S.C., 2000. *Computational electrodynamics: the finite-difference time-domain method*, 2nd ed., Artech House, Norwood, MA.
- Van Renterghem, T. & Botteldoren, D., 2003. Numerical simulation of the effect of trees on downwind noise barrier performance, *Acust. Acta. Acust.*, 89, 764-778.
- Walker, K., de Groot-Hedlin, C., Hedlin, M., Vergoz, J. & Le Pichon, A., 2010. The 2008 February 19 Oregon Bolide Located with Dense Seismometer Networks, *J. Geophys. Res.*, in press.

- Whitaker, R. W. & Mutschlecner, J. P., 2008. A comparison of infrasound signals refracted from stratospheric and thermospheric altitudes, *J. Geophys. Res.*, 113, D08117, doi:10.1029/2007JD008852.
- Yee, K.S., 1966. Numerical solution of initial boundary value problems involving Maxwell's equations in isotropic media, *IEEE trans. Antennas and Propagation*, 14, 302-307.